

Changes in Aridity in Response to the Global Warming Hiatus

Xiaodan GUAN, Jianping HUANG*, and Ruixia GUO

*Key Laboratory for Semi-Arid Climate Change of the Ministry of Education,
College of Atmospheric Sciences, Lanzhou University, Lanzhou 730000*

(Received April 21, 2016; in final form September 23, 2016)

ABSTRACT

The global warming slowdown or warming hiatus, began around the year 2000 and has persisted for nearly 15 years. Most studies have focused on the interpretation of the hiatus in temperature. In this study, changes in a global aridity index (AI) were analyzed by using a newly developed dynamical adjustment method that can successfully identify and separate dynamically induced and radiatively forced aridity changes in the raw data. The AI and Palmer Drought Severity Index produced a wetting zone over the mid-to-high latitudes of the Northern Hemisphere in recent decades. The dynamical adjustment analysis suggested that this wetting zone occurred in response to the global warming hiatus. The dynamically induced AI (DAI) played a major role in the AI changes during the hiatus period, and its relationships with the North Atlantic Oscillation (NAO), Pacific Decadal Oscillation (PDO), and Atlantic Multi-decadal Oscillation (AMO) also indicated that different phases of the NAO, PDO, and AMO contributed to different performances of the DAI over the Northern Hemisphere. Although the aridity wetting over the mid-to-high latitudes may relieve long-term drying in certain regions, the hiatus is temporary, and so is the relief. Accelerated global warming will return when the NAO, PDO, and AMO revert to their opposite phases in the future, and the wetting zone is likely to disappear.

Key words: hiatus, aridity index, dynamically induced aridity index, wetting

Citation: Guan, X. D., J. P. Huang, and R. X. Guo, 2017: Changes in aridity in response to the global warming hiatus. *J. Meteor. Res.*, **31**(1), 117–125, doi: 10.1007/s13351-017-6038-1.

1. Introduction

The warming hiatus is one of the most striking climate events in the early 21st century and has attracted global attention due to its apparent contradiction to human-induced global warming theories. The observed temperature throughout the hiatus period has challenged the role of greenhouse gases (GHGs) in global warming over the past century. Guemas et al. (2013) claimed that the hiatus was induced by ocean heat changes. Excess heat absorbed by the climate system does not necessarily warm earth's surface; instead, this heat can be stored in the ocean (Otterå et al., 2010; Foster and Rahmstorf, 2011). Meehl et al. (2011) proposed that varying trends at different ocean depths between hiatus and non-hiatus periods could lead to the warming hiatus. This theory was supported by Kosaka and Xie (2013), which re-

vealed changes in the global mean surface air temperature (SAT) and a recent pause of warming in the Geophysical Fluid Dynamics Laboratory Coupled Model.

In the early 2010s, Wang et al. (2010a, b, 2011) recognized the hiatus will become an attractive issue in the community of climate change, and started to study the hiatus (Wang et al., 2013a, b, 2014). Recently, Guan et al. (2015a) employed an adapted raw SAT method (Wallace et al., 2012) and extracted the dynamically induced temperature from the raw SAT, which indicated opposite effects of dynamically induced and radiatively forced temperatures in the hiatus period. Additionally, Guan et al. (2015a) proposed that anthropogenic factors could have contributed to the SAT increase that offset the cooling effect of dynamically induced temperature. The dynamically induced cooling effects in the process of the warming hiatus are also associated with internal climate

Supported by the National Natural Science Foundation of China (41575006, 41521004, and 91637312) and China 111 Project (B13045).

*Corresponding author: hjp@lzu.edu.cn.

©The Chinese Meteorological Society and Springer-Verlag Berlin Heidelberg 2017

variability modes. These modes have been found to excite a global decadal modulated oscillation (DMO) and change the asymmetric meridional thermal forcing (MTF) and zonal thermal forcing (ZTF) (Huang et al., 2016). The strongest DMO modulation effect on the SAT appeared when both weaker (stronger) MTF and stronger (weaker) ZTF occurred simultaneously. The current hiatus is the result of a downward DMO combined with a weaker MTF and stronger ZTF.

Although the near 15-yr global warming hiatus has been widely recognized, a series of climate changes associated with the warming hiatus have not received widespread attention from the research community. As a traditional topic in climate change (Zhou et al., 2014; Dai et al., 2015; Zhou and Chen, 2015), regional aridity that occurred as a large-scale drying trend in the period of enhanced warming has been studied via climatology datasets (Huang et al., 2012) and direct measurements (Huang et al., 2008; Guan et al., 2009; Wang et al., 2010). However, the aridity created a change during the hiatus decade compared with the accelerated-warming period beforehand. A number of results have focused on the historical wetting/drying trend (Hoerling et al., 2006; Huang et al., 2015), but there have been few studies on aridity index (AI) change in the hiatus period. In this study, we examined aridity changes associated with the warming hiatus by using a recently developed methodology that can successfully identify dynamically induced and radiatively forced aridity changes from raw AI data. We introduce the data and methodology in Section 2. The aridity change during the hiatus, as well as the possible causes, are described in Section 3. Conclusions and discussion are presented in Section 4.

2. Data and methodology

2.1 Data

In this study, we used monthly-mean SAT data from the Climate Research Unit (CRU) TS3.21 dataset, provided by the University of East Anglia. The data cover the period 1901–2012 (Mitchell and Jones, 2005) and have a resolution of $0.5^\circ \times 0.5^\circ$. This gridded dataset is based on an archive of monthly-mean temperature provided by more than 4000 weather stations distributed around the world.

The precipitation data used in this study were obtained from the Climate Prediction Center of the National Centers for Environmental Prediction (Chen et al., 2002). This dataset is labeled as the Precipitation Reconstruction over Land (PREC/L) dataset, has a spatial resolu-

tion of $0.5^\circ \times 0.5^\circ$, and covers the period 1948–2008. Gauge observations of over 17000 stations and two large datasets (the Global Historical Climatology Network version 2, and the Climate Anomaly Monitoring System) were collected in the PREC/L dataset, which aims to update the PREC/L with a sufficient number of stations regularly in near real time. The potential evapotranspiration (PET) dataset was calculated based on the Penman-Monteith algorithm, which is derived from physical principles and is superior to empirically based formulations that usually consider only the effects of temperature and radiation. The Penman-Monteith algorithm considers many meteorological parameters related to evapotranspiration, such as net radiation, relative humidity, wind speed, and temperature data, as well as information on vegetation characteristics (Allen et al., 1998):

$$\text{PET} = \frac{0.408\Delta(R_n - G) + \gamma \frac{900}{T_a + 273} u_2 (e_s - e_a)}{\Delta + \gamma(1 + 0.34u_2)}, \quad (1)$$

where R_n is the net radiation at the crop surface ($\text{MJ m}^{-2} \text{day}^{-1}$), G is the soil heat flux density at the soil surface ($\text{MJ m}^{-2} \text{day}^{-1}$), T_a is the daily-mean air temperature at 2-m height ($^\circ\text{C}$), u_2 is the wind speed at 2-m height (m s^{-1}), e_s is the saturation vapor pressure at 2-m height (kPa), e_a is the actual vapor pressure at 2-m height (kPa), Δ is the slope of the vapor pressure–temperature curve ($\text{kPa } ^\circ\text{C}^{-1}$), and γ is the psychrometric constant ($\text{kPa } ^\circ\text{C}^{-1}$). The data for net surface radiation (including shortwave and longwave radiation), specific humidity, wind speed, and soil heat flux density, were from the data product of the Global Land Data Assimilation System (GLDAS). The solar radiation data were corrected based on two global radiation products (Sheffield et al., 2006). The observation-based climatological method developed by the CRU (Mitchell and Jones, 2005) was also applied to the specific humidity and wind speed data.

The AI (Feng and Fu, 2013) was calculated as the annual precipitation divided by the PET derived from Eq. (1). Another type of AI is the Palmer Drought Severity Index (PDSI). Dai's self-calibrated PDSI dataset (sc_PDSI_pm; <http://www.cgd.ucar.edu/cas/adai/data-dai.html>) (Dai, 2011a, b) is widely used to study the global aridity changes induced by the El Niño–Southern Oscillation (Wang et al., 2014). The PDSI is calculated from a water balance model that is forced by observed precipitation and temperature data and widely used to study aridity changes. The revised sc_PDSI_pm offers an improved spatial comparability calculation with a more realistic estimate of PET, which improves its applicability for global warming scenarios (Dai, 2011a).

Model simulation outputs were also used in this study. The datasets for precipitation and PET from the historical simulations of 20 CMIP5 climate models were used in this study (Table 1), together with the +4.5 W m⁻² Representative Concentration Pathway (RCP4.5) runs, to assess the correlation with the observational dataset, which are based on medium-to-low scenario simulations in CMIP5 for the RCP 2005–2008 simulation (Taylor et al., 2012; Zhao and Dai, 2015). Observed sea level pressure (SLP) data were obtained from the National Oceanic and Atmospheric Administration and the Cooperative Institute for Research in Environmental Sciences 20th Century Reanalysis package version 2, which has a spatial resolution of 2° × 2° and covers the period 1901–2011 (Compo et al., 2011). The North Atlantic Oscillation (NAO), Pacific Decadal Oscillation (PDO), and Atlantic Multi-decadal Oscillation (AMO) indexes were downloaded from the Climate Explorer (<http://climexp.knmi.nl/>).

2.2 Dynamical adjustment method

The dynamical adjustment method was first proposed by Wallace et al. (2012) to examine the causes of accelerating warming over the mid-to-high latitude regions of the Northern Hemisphere. It has been used to study the warming hiatus in recent decades in the cold season (November–March; Guan et al., 2015a). It has been shown that the greatest effect of this method stems from subtracting the dynamic and regional radiative temperature from the raw data. First, the method is performed by

correlating the SAT at each grid point with standardized SLP poleward of 20°N to form a one-point correlation map expressing the relationship between SLP and SAT. Second, the standardized SLP field is projected onto the correlation pattern, weighting each grid point by the cosine of latitude to obtain a time-varying index of the correlation pattern; namely, the predictor. Third, regress the predictor out of both the SAT and SLP field to obtain the dynamically induced SAT. Repeat the above steps with the residual SAT time series and the residual SLP field.

By applying the steps described above, the raw temperature T was divided into two parts, as expressed by

$$T = T_{\text{dyn}} + T_{\text{adj}}, \quad (2)$$

where T_{dyn} and T_{adj} are the time series of the dynamically induced temperature and adjusted (radiatively forced) temperature, respectively. The dynamically induced part is attributable to changes in atmospheric circulation patterns, and the adjusted part is associated with radiatively forced factors, which is considered to be a result of GHG accumulation, stratospheric ozone depletion, volcanic eruption, aerosol emissions, and local anthropogenic forcing. It has been demonstrated that the enhanced semi-arid warming in East Asia is due to the radiatively forced warming (Guan et al., 2015b). As the SLP contains the signals of semi-permanent atmospheric activity centers in the mid-to-high latitudes of the Northern Hemisphere, such as the NAO and the North Pacific Oscillation (NPO), these decadal and interdecadal signals of internal dynamic effects in the system can be subtracted by partial regression by using this method. As the dynamical adjustment method only works for the cold season, and the raw SAT is almost the same as the radiatively forced SAT in the warm season (May–September), the annual mean dynamically induced SAT is nearly equal to that of the cold season mean. Therefore, we employed the dynamical adjustment method to the annual AI to analyze the process of aridity change in the recent hiatus period. According to the dynamical adjustment method, the AI was divided into two components: the dynamically induced AI (DAI) and the radiatively forced AI (RAI).

3. Results and analysis

The hiatus has attracted considerable attention from the public since it appeared around the year 2000. The stoppage in the temperature increase began around 2000, as shown in Fig. 1a. In the Northern Hemisphere, the temperature time series from 1902 to 2012 (Fig. 1a) indicates a distinct pause during the last decade in terms of the annual-mean temperature, with a decrease in temper-

Table 1. CMIP5 models examined in this study

Model name	Modeling center
BCC_CSM1.1	Beijing Climate Center, China
CanESM2	Canadian Centre for Climate, Canada
CCSM4	National Center for Atmospheric Research, USA
CNRM-CM5	Centre National de Recherches Météorologiques, France
CSIRO Mk3.6.0	Commonwealth Scientific and Industrial Research, Australia
GFDL CM3	Geophysical Fluid Dynamics Laboratory, USA
GFDL-ESM2G	Geophysical Fluid Dynamics Laboratory, USA
GFDL-ESM2M	Geophysical Fluid Dynamics Laboratory, USA
GISS-E2-R	Goddard Institute for Space Studies, NASA, USA
HadGEM2-CC	Met Office Hadley Centre, UK
HadGEM2-ES	Met Office Hadley Centre, UK
INM-CM4.0	Institute for Numerical Mathematics, Russia
IPSL-CM5A-LR	L'Institut Pierre-Simon Laplace, France
IPSL-CM5A-MR	L'Institut Pierre-Simon Laplace, France
MIROC-ESM	Japan Agency for Marine–Earth Science and Technology, Japan
MIROC-ESM-CHEM	Japan Agency for Marine–Earth Science and Technology, Japan
MIROC5	Atmosphere and Ocean Research Institute, Japan
MPI-ESM-LR	Max Planck Institute for Meteorology, Germany
MRI-CGCM3	Meteorological Research Institute, Japan
NorESM1-M	Norwegian Climate Centre, Norway

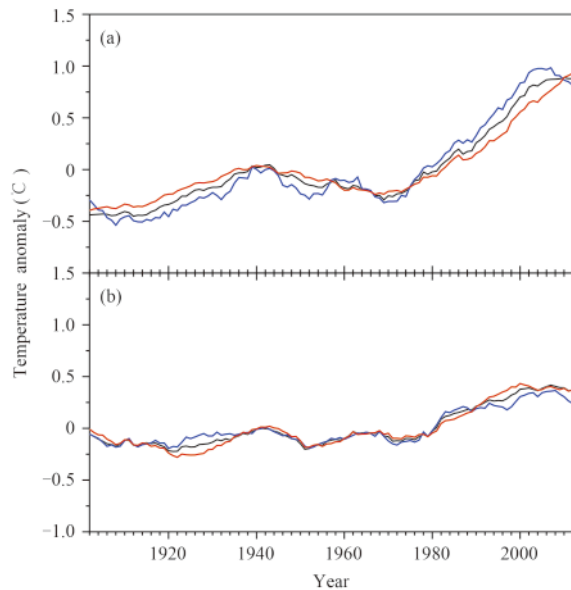


Fig. 1. Regional-mean temperature anomaly time series, based on the 11-yr running mean from 1902 to 2012 in the (a) Northern Hemisphere and (b) Southern Hemisphere, in terms of the annual mean (black), cold season (November–March, blue), and warm season (May–September, red).

ature in the cold season and an increase of temperature in the warm season. Prior to the hiatus, i.e., in the period 1970–2000, the SAT in both the cold and warm seasons increased continuously, maintaining high temperatures. For the Southern Hemisphere (Fig. 1b), the change in annual-mean SAT in the cold season and warm season exhibited a clear temperature increase in 1970–2000, and a stoppage in the temperature increase in the hiatus period—similar to the temperature changes in the Northern Hemisphere, but with a smaller amplitude. Therefore, the temporal SAT trend in the cold season led to an annual-mean SAT change, particularly in the Northern Hemisphere.

Further exploration of the warming hiatus has revealed additional changes during this period. For example, sea ice continued to decline rapidly, warm temperature extremes intensified (Seneviratne et al., 2014), and extreme events became more frequent (Sillmann et al., 2014). The AI also exhibited a clear change during the hiatus period, as shown in Fig. 2. The observed AI appeared flat from 1948 to the late 1970s in the Northern Hemisphere (Fig. 2a), whereas a notable decrease occurred in the accelerated warming period from the late 1970s to 2000, and the data exhibited an increasing trend around 2002 until the present day. However, the 20 CMIP5 models' ensemble-mean AI exhibited a flat change and showed that the CMIP5 time series were considerably smoother than the observed AI curve. The sim-

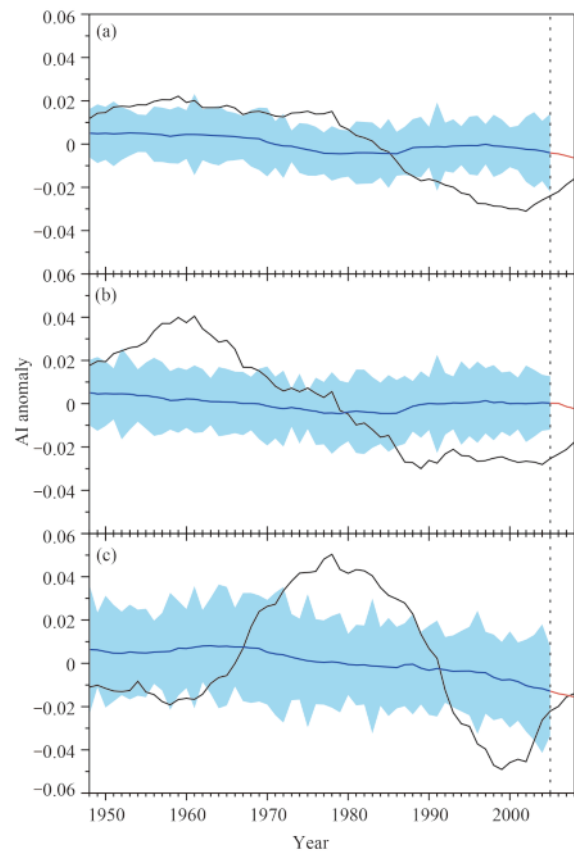


Fig. 2. Regional-mean time series of observed (black) and CMIP5 ensemble-mean (blue) AI anomalies, based on the 11-yr running mean over the (a) Northern Hemisphere, (b) Eurasia, and (c) North America, from 1948 to 2008. The shaded area denotes the standard deviation of the CMIP5 AI values. The red parts of the curves signify regional-mean AI projections drawn from RCP4.5.

ulations underestimated the AI change and exhibited a slight decreasing trend over the Northern Hemisphere during the past 60 years. This notable discrepancy between the observed and simulated AI results demonstrates the difficulty in modeling AI variability trends, specifically, the enhanced decreasing trend during 1970–2000 and the increasing trend in the hiatus period (i.e., 2000–2008). The observed area-average AI in Eurasia (Fig. 2b) exhibited a significant decrease from the 1960s until 1990; and thereafter, the AI plateaued and subsequently increased in the most recent decade. In addition, the observed AI over North America (Fig. 2c) demonstrated a more pronounced recovery during the hiatus period. A clear increase in the AI appeared in the period 1960–1980, but decreased during the period 1980–1998. In addition, a new increase in the AI began around 2000, which was also the start of the warming hiatus.

To emphasize the change in AI between the warming

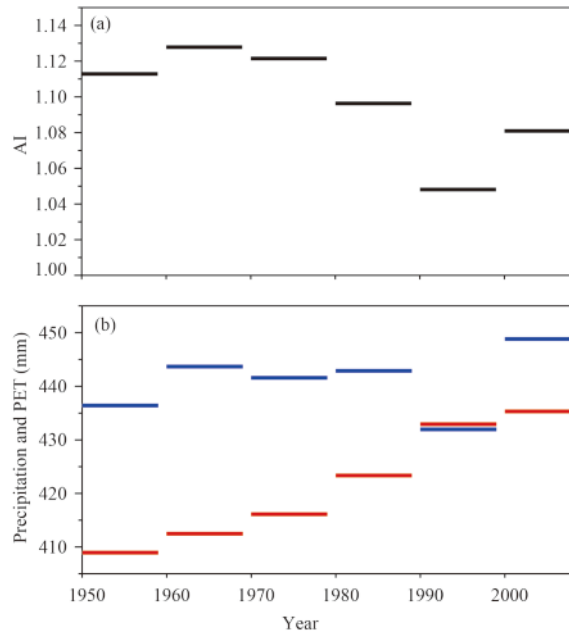


Fig. 3. Decadal variability of (a) AI and (b) precipitation (blue) and PET (red) during 1948–2008.

and hiatus decades, the decadal-mean AI is shown in Fig. 3a, which is expressed as the variability of mean values over each period of 10 years. As can be seen, the AI has exhibited a continuous decreasing trend since the 1950s. The AI reached its lowest value of about 1.05 in the 1990s, but displayed a clear recovery in the recent hiatus period. The decadal variability of precipitation and PET in Fig. 3b shows that precipitation had a relatively flat change, except in the 1990s. Precipitation in the 1990s took on a notably lower value than in the previous dec-

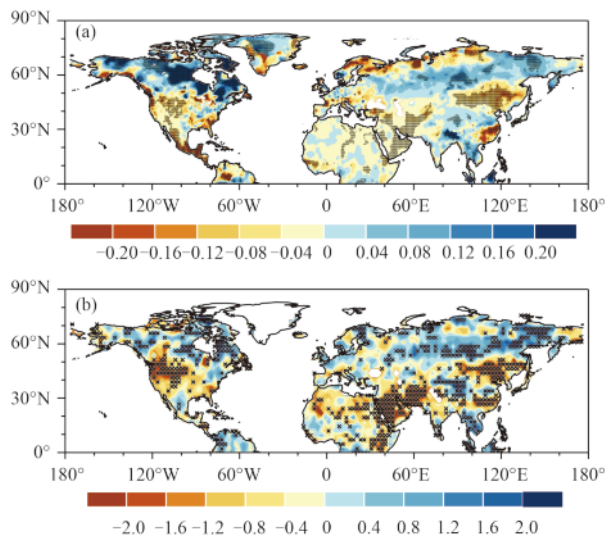


Fig. 4. Differences between the periods 2000–2008 and 1991–1999 in terms of the (a) AI and (b) PDSI. Stippling denotes the 90% statistical confidence level according to the two-tailed Student’s *t*-test.

ade (the 1980s) and the following decade (the 2000s) (Fig. 3b). PET exhibited a continuous increase from the 1950s to the present day, with a notable increase in the 1980s and 1990s, which were the two decades of enhanced warming, relative to the 1970s.

Figure 4 shows the spatial distribution of the difference between the averaged anomalies during 2000–2008 and those during 1991–1999 for the AI (Fig. 4a) and PDSI (Fig. 4b). Figure 4a shows that northern and southern North America exhibited opposite patterns, with drying in the United States and wetting over Canada and Greenland. Over Eurasia, a distinct drying trend appeared in the high-latitude areas across the Arctic Ocean, Mongolia, and northeastern and southeastern China, and wetting happened in the 50°–70°N belt and northwestern China. The continental reversing trend of the spatial distribution of AI variation shown in Fig. 4a suggests that the AI changes during the hiatus period were concentrated in the mid-to-high latitude areas of the Northern Hemisphere. The majority of the area with a 90% significance level was located in northeastern China, between Europe and Africa, in northern Canada, and in western North America. Figure 4b shows the PDSI differences between the hiatus period and the preceding decade over the Northern Hemisphere (excluding Greenland), revealing a change pattern similar to that of the AI. A decrease in the frequency of drought events appeared in the high latitudes of the Northern Hemisphere, and the majority of the area with increased frequency was located in the northwestern United States, northeastern China, and the Iranian Plateau, with a 90% confidence level. The AI in the hiatus period relative to the previous decade demonstrated that the drying over the mid-to-high latitudes, which used to be rapidly changing aridity areas, was diminished in the hiatus period.

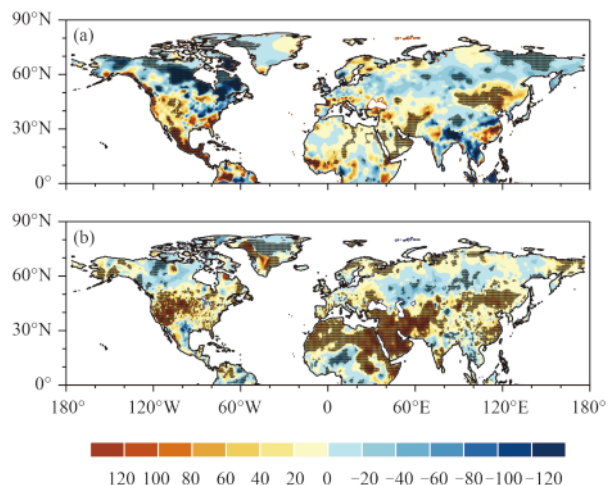


Fig. 5. As in Fig. 4, but for (a) precipitation (mm) and (b) PET (mm).

Figure 5 shows the differences between the periods of 2000–2008 and 1991–1999 in terms of precipitation (Fig. 5a) and PET (Fig. 5b). The increasing precipitation areas were distributed over the mid-to-high latitudes of the Northern Hemisphere, especially in Canada, where a high center appeared in eastern Canada. The decreasing centers were located in northeastern China, the area between Europe and Africa, and the United States. Most areas in the Northern Hemisphere experienced an increasing trend; the two increasing centers were located in the adjacent area between Europe and Africa and in the United States. The decreases occurred over the centers of Canada and Russia. Compared with Fig. 4a, the distributions of both precipitation and PET indicated a wetting belt over high latitudes.

Figure 6 illustrates the correlation coefficients between the DAI and annual-mean temperature. It exhibits a negative pattern with major influences distributed in East Asia, Canada, central America, southern Europe, and the area surrounding Africa. Positive patterns were located in the high latitudes of Asia, western America, and central Africa on small scales. The dominant negative relationship confirms the temperature effect in the process of dynamic AI change, and demonstrates that the AI change in recent decades had a close relationship with temperature change. To explore the dynamically induced effect on AI change, we calculated the differences between the periods of 2000–2008 and 1991–1999 in terms of the DAI (Fig. 7a), and in terms of the DAI time series for the Northern Hemisphere (Fig. 7b), Eurasia (Fig. 7c), and North America (Fig. 7d). We can see a wetting over the mid-to-high latitude regions of Eurasia, Greenland, and Canada (Fig. 7a). At the same time, a drying region appeared over North America, southern Europe, Mongolia, and eastern China, with a confidence level of 90%. The consistent distribution of DAI with the raw AI difference (Fig. 4a) indicates that DAI dominated the change of the AI on a large scale. The pattern of wetting and drying poleward of 20°N has changed the regional ecological

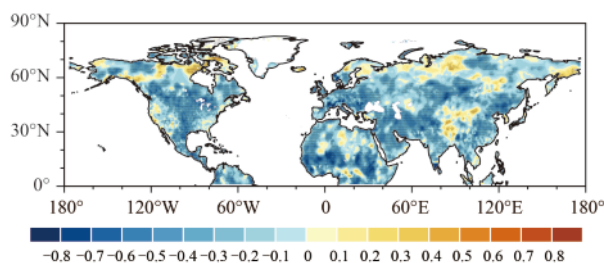


Fig. 6. Correlation coefficients between the DAI and raw annual-mean temperature in the period 1948–2008. Stippling indicates the 95% confidence level according to the two-tailed Student's *t*-test.

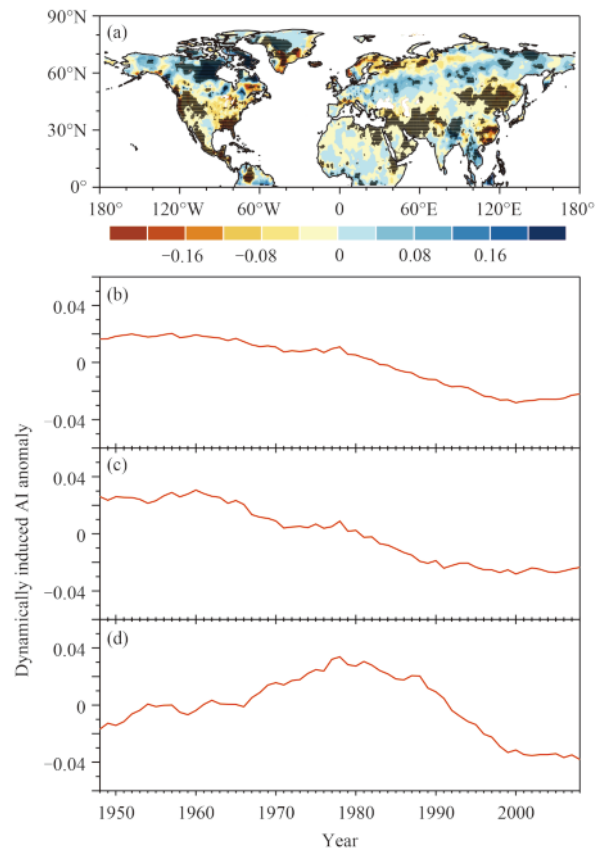


Fig. 7. (a) Differences between the period 2000–2008 and 1991–1999 in terms of the DAI. (b–d) Regional-mean time series of DAI anomalies, based on the 11-yr running mean for the (b) Northern Hemisphere, (c) Eurasia, and (d) North America, from 1948 to 2008. Stippling denotes the 90% statistical confidence level according to the two-tailed Student's *t*-test.

environment (Shugart and Woodward, 2011). The area-averaged DAI time series showed a slight increase in the average AI over the Northern Hemisphere during the hiatus period after a long-term decreasing trend (Fig. 7b). A similar trend was found over Eurasia (Fig. 7c). The AI time series for North America (Fig. 7d) peaked around 1980 before decreasing abruptly and ultimately plateauing around 2000. The variability of the AI over different areas displayed a stoppage in the continuously decreasing AI in the most recent decade over the continent, suggesting that the rapid aridity in the 1990s may have been relieved in the hiatus period.

As illustrated in Fig. 7a, the major differences in the DAI between the two periods indicated that wetting was led by the DAI. The DAI change in response to the warming hiatus might have been controlled by global-scale systems, such as the NAO, PDO, and AMO. Therefore, we calculated the correlation coefficients of the DAI with the NAO, PDO, and AMO, as shown in Figs. 8–10. Figure 8a presents the time series of the NAO in

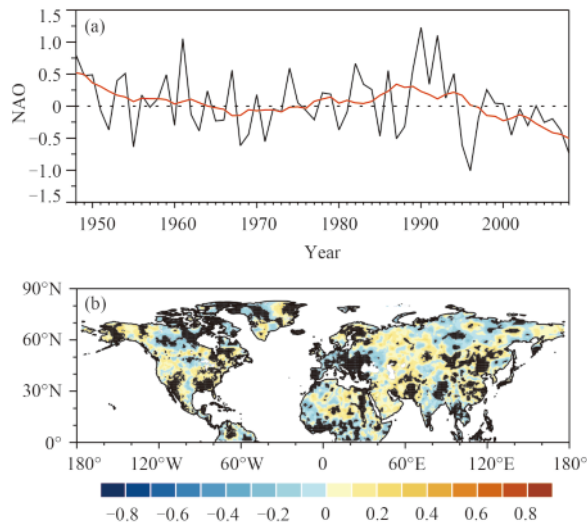


Fig. 8. (a) Time series of the NAO during 1948–2008, in which the red curve represents the 11-yr running mean. (b) Spatial distribution of the correlation coefficients between the detrended NAO and the detrended DAI in the period 1948–2008. Stippling indicates the 95% statistical confidence level according to the two-tailed Student’s *t*-test.

the period 1948–2008, and illustrates that the phase of the NAO changed during this period. A positive phase occurred in the 1950s, but the trend became negative in the 1960s. Starting from the 1970s, it exhibited the strongest positive phase until the 2000s, but switched to negative phase in 2000. Figure 8b shows the distribution of the correlation coefficients between the NAO and the DAI. Major negative areas were distributed over the mid-to-high latitude regions of Asia, southern Europe, northern North America, poleward of 50°N, and south of 25°N in Africa. The positive areas were distributed in Eurasia between 30° and 50°N, North Africa, and North Amer-

ica. This observation illustrates the strong influence of the NAO on the DAI over the Eurasian and North American continents. Because the NAO showed a transition from positive in the enhanced warming period to negative in the warming hiatus period, the negative correlation coefficients over the mid-to-high latitude regions of Asia, southern Europe, northern North America, poleward of 50°N, and south of 25°N in Africa represent the wetting effect on the DAI. The positive correlation coefficients indicate a drying effect on the DAI in Eurasia between 30° and 50°N, and in certain regions of both North Africa and the United States.

Figure 9a displays the time series of the PDO during 1948–2008, revealing that the PDO was in a negative phase in the 1950s and changed swiftly to a positive phase around 1978 before returning back to a negative pattern around the 2000s until the present day. Previous simulation results (Meehl et al., 2011) show that the PDO bears a close relationship with the frequency of La Niña events. Figure 9b shows the correlation coefficients between the PDO and the DAI. Negative correlation was found over northwestern North America, most of Greenland, the northeast of Eurasia, poleward of 60°N, and south of Africa. The positive correlation coefficients were distributed in North America, especially the western part and central Eurasia, with 95% statistical confidence. Conversely, the negative correlation coefficients represented a wetting effect on the DAI in northwestern USA, most of Greenland, northeastern Eurasia, poleward of 60°N, and south of Africa, in the hiatus period. Compared with Fig. 8b, the correlation coefficients between the DAI and PDO were higher than those between the DAI and NAO.

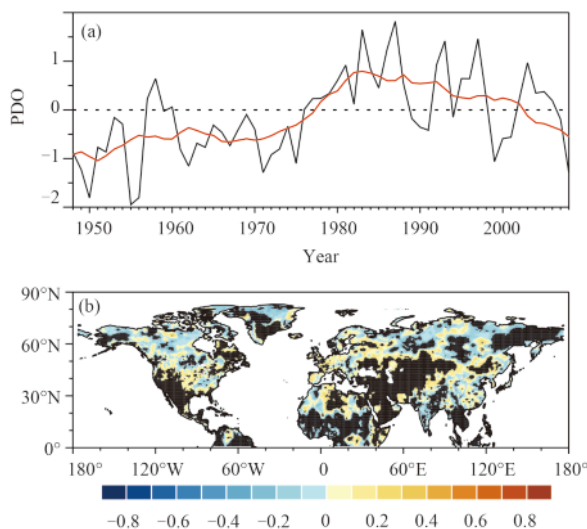


Fig. 9. As in Fig. 8, but for the PDO.

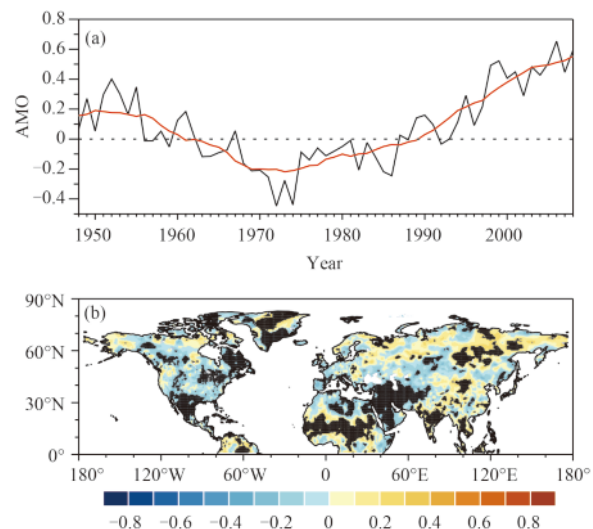


Fig. 10. As in Fig. 8, but for the AMO.

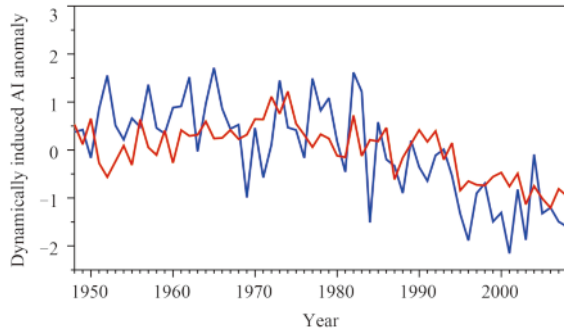


Fig. 11. Comparison of the time series of the DAI poleward of 20°N (blue) and its regression onto the NAO, PDO, and AMO (red).

In addition to the NAO and PDO, the AMO is an effective index for measuring dynamic activities. Figure 10a illustrates that the AMO maintained an increasing trend in the hiatus period. The distribution of the correlation coefficients between the DAI and AMO (Fig. 10b) exhibited a negative relationship over most of North America, western Eurasia, and the area between Eurasia and Africa, indicating a drying effect on these areas in the hiatus period. A positive relationship was observed over northern Greenland, northeastern Eurasia, most of China, and central Africa, which suggests a wetting effect of the AMO in the hiatus period.

To illustrate the roles of the NAO, PDO, and AMO in the variability of the DAI on the decadal scale, the DAI regressed onto the three indices is illustrated in Fig. 11. This figure compares the time series of the DAI with the regressed DAI and illustrates that the time series of the DAI poleward of 20°N can be approximately described by regression analysis. A simple three-variable regression equation can be derived to represent the mean DAI change in the Northern Hemisphere using the NAO, PDO, and AMO indices as regression variables:

$$\text{DAI} = 0.20 \times \text{NAO} - 0.22 \times \text{PDO} - 0.46 \times \text{AMO}. \quad (3)$$

A comparison of the time series between the regressed DAI and DAI over the Northern Hemisphere illustrates that the regressed DAI can capture the major features of the DAI change, indicating a consistent decreasing change. The contributions of the NAO, PDO, and AMO to the DAI poleward of 20°N were 21%, 21.3%, and 57.7%, respectively. The dominant role of the AMO over the long term in the regression illustrates that, relative to the low value of the spatial distribution of the correlation coefficients between the AMO and the DAI in Fig. 10, the AMO is a dynamic factor for the multi-decadal variability of climate change in the time series.

4. Conclusions and discussion

This study revealed that the AI experienced a wetting reversal in the recent warming hiatus period, and similar spatial distributions of the AI and PDSI changes demonstrated that the aridity pattern and drought frequency had consistent drying/wetting changes for most regions. A correlation analysis of the DAI with the NAO, PDO, and AMO suggested that the DAI is dominated primarily by these three major oscillations. The contributions of the NAO, PDO, and AMO to the DAI in the period from 1948–2008 were 21.0%, 21.3%, and 57.7%, respectively. The opposite phases of the NAO and PDO led to a different distribution of the AI.

The recent wetting trend associated with the warming hiatus that has affected the Northern Hemisphere is due to dynamic processes. These processes have resulted in wetting trends over the mid-to-high latitude areas of the Northern Hemisphere and highlighted the effect of the warming hiatus on global climate change. The change in the AI during the warming hiatus period with respect to the previous period of rapidly accelerating warming is a signal of the warming hiatus effect, indicating that the influence of the warming hiatus is not limited to temperature change; the AI wetting can also be considered to be a “hiatus effect” resulting from the stoppage in the temperature increase. The “hiatus effect” has emerged as an accompanied feature of warming hiatus, encompassing snow, ice, precipitation, and PET, among other factors. Additional investigations on the hiatus effect are needed, as the AI level has plateaued in the most recent warming hiatus period, and dry-wet patterns have changed after the stoppage in the temperature increase. However, global climate change will take on a new scenario in the future if the dynamic effect returns to a positive pattern.

REFERENCES

- Allen, R. G., L. S. Pereira, D. Raes, et al., 1998: Crop evapotranspiration-guidelines for computing crop water requirements. FAO Irrigation and Drainage Paper 56, FAO, Rome.
- Chen, M. Y., P. P. Xie, J. E. Janowiak, et al., 2002: Global land precipitation: A 50-yr monthly analysis based on gauge observations. *J. Hydrometeorol.*, **3**, 249–266, doi: 10.1175/1525-7541(2002)003<0249:GLPAYM>2.0.CO;2.
- Compo, G. P., J. S. Whitaker, P. D. Sardeshmukh, et al., 2011: The twentieth century reanalysis project. *Quart. J. Roy. Meteor. Soc.*, **137**, 1–28, doi: 10.1002/qj.776.
- Dai, A. G., 2011a: Characteristics and trends in various forms of the Palmer Drought Severity Index during 1900–2008. *J. Geophys. Res. Atmos.*, **116**, doi: 10.1029/2010JD015541.
- Dai, A. G., 2011b: Drought under global warming: A review. *WIREs Climate Change*, **2**, 45–65, doi: 10.1002/wcc.81.
- Dai, A. G., J. C. Fyfe, S. P. Xie, et al., 2015: Decadal modulation

- of global surface temperature by internal climate variability. *Nat. Climate Change*, **5**, 555–559, doi: 10.1038/nclimate2605.
- Feng, S., and Q. Fu, 2013: Expansion of global drylands under a warming climate. *Atmos. Chem. Phys.*, **13**, 10081–10094, doi: 10.5194/acpd-13-10081-2013.
- Foster, G., and S. Rahmstorf, 2011: Global temperature evolution 1979–2010. *Environ. Res. Lett.*, **6**, 044022, doi: 10.1088/1748-9326/6/4/044022.
- Guan, X. D., J. P. Huang, N. Guo, et al., 2009: Variability of soil moisture and its relationship with surface albedo and soil thermal parameters over the Loess Plateau. *Adv. Atmos. Sci.*, **26**, 692–700, doi: 10.1007/s00376-009-8198-0.
- Guan, X. D., J. P. Huang, R. X. Guo, et al., 2015a: The role of dynamically induced variability in the recent warming trend slowdown over the Northern Hemisphere. *Sci. Rep.*, **5**, 12669, doi: 10.1038/srep12669.
- Guan, X. D., J. P. Huang, R. X. Guo, et al., 2015b: Role of radiatively forced temperature changes in enhanced semi-arid warming in the cold season over East Asia. *Atmos. Chem. Phys.*, **15**, 13777–13786, doi: 10.5194/acp-15-13777-2015.
- Guemas, V., F. J. Doblas-Reyes, I. Andreu-Burillo, et al., 2013: Retrospective prediction of the global warming slowdown in the past decade. *Nat. Climate Change*, **3**, 649–653, doi: 10.1038/nclimate1863.
- Hoerling, M., J. Hurrell, J. Eischeid, et al., 2006: Detection and attribution of twentieth-century northern and southern African rainfall change. *J. Climate*, **19**, 3989–4008, doi: 10.1175/JCLI3842.1.
- Huang, J., X. Guan, and F. Ji, 2012: Enhanced cold-season warming in semi-arid regions. *Atmos. Chem. Phys.*, **12**, 5391–5398, doi: 10.5194/acp-12-5391-2012.
- Huang, J. P., M. X. Ji, Y. K. Xie, et al., 2015: Global semi-arid climate change over last 60 years. *Climate Dyn.*, **46**, 1131–1150, doi: 10.1007/s00382-015-2636-8.
- Huang, J. P., W. Zhang, J. Q. Zuo, et al., 2008: An overview of the semi-arid climate and environment research observatory over the Loess Plateau. *Adv. Atmos. Sci.*, **25**, 906–921, doi: 10.1007/s00376-008-0906-7.
- Huang, J. P., Y. K. Xie, X. D. Guan, et al., 2016: The dynamics of the warming hiatus over the Northern Hemisphere. *Climate Dyn.*, 1–18. doi: 10.1007/s00382-016-3085-8.
- Kosaka, Y., and S. P. Xie, 2013: Recent global-warming hiatus tied to equatorial Pacific surface cooling. *Nature*, **501**, 403–407, doi: 10.1038/nature12534.
- Meehl, G. A., J. M. Arblaster, J. T. Fasullo, et al., 2011: Model-based evidence of deep-ocean heat uptake during surface-temperature hiatus periods. *Nat. Climate Change*, **1**, 360–364, doi: 10.1038/nclimate1229.
- Mitchell, T. D., and P. D. Jones, 2005: An improved method of constructing a database of monthly climate observations and associated high-resolution grids. *Int. J. Climatol.*, **25**, 693–712, doi: 10.1002/joc.1181.
- Otterå, O. H., M. Bentsen, H. Drange, et al., 2010: External forcing as a metronome for Atlantic multidecadal variability. *Nat. Geosci.*, **3**, 688–694, doi: 10.1038/ngeo955.
- Seneviratne, S. I., M. G. Donat, B. Mueller, et al., 2014: No pause in the increase of hot temperature extremes. *Nat. Climate Change*, **4**, 161–163, doi: 10.1038/nclimate2145.
- Sheffield, J., G. Goteti, and E. F. Wood, 2006: Development of a 50-yr high-resolution global dataset of meteorological forcings for land surface modeling. *J. Climate*, **19**, 3088–3111, doi: 10.1175/JCLI3790.1.
- Shugart, H. H., and F. I. Woodward, 2011: *Global Change and the Terrestrial Biosphere: Achievements and Challenges*. John Wiley & Sons, 242 pp.
- Sillmann, J., M. G. Donat, J. C. Fyfe, et al., 2014: Observed and simulated temperature extremes during the recent warming hiatus. *Environ. Res. Lett.*, **9**, 064023, doi: 10.1088/1748-9326/9/6/064023.
- Taylor, K. E., R. J. Stouffer, G. A. Meehl, 2012: An overview of CMIP5 and the experiment design. *Bull. Amer. Meteor. Soc.*, **93**, 485–498, doi: 10.1175/BAMS-D-11-00094.1.
- Wallace, J. M., Q. Fu, B. V. Smoliak, et al., 2012: Simulated versus observed patterns of warming over the extratropical Northern Hemisphere continents during the cold season. *Proc. Natl. Acad. Sci. U. S. A.*, **109**, 14337–14342, doi: 10.1073/pnas.1204875109.
- Wang, G. Y., J. P. Huang, W. D. Guo, et al., 2010: Observation analysis of land–atmosphere interactions over the Loess Plateau of Northwest China. *J. Geophys. Res. Atmos.*, **115**, D00K17, doi: 10.1029/2009JD013372.
- Wang, S. S., J. P. Huang, Y. L. He, et al., 2014: Combined effects of the Pacific decadal oscillation and El Niño–Southern Oscillation on global land dry–wet changes. *Sci. Rep.*, **4**, 6651, doi: 10.1038/srep06651.
- Wang, S. W., X. Y. Wen, Y. Luo, et al., 2010a: Does the global warming pause in the last decade: 1999–2008? *Adv. Climate Change Res.*, **1**, 49–54, doi: 10.3724/SP.J.1248.2010.00049.
- Wang, S. W., Q. S. Ge, F. Wang, et al., 2010b: Key issues on debating about the global warming. *Adv. Earth Sci.*, **25**, 656–665. (in Chinese)
- Wang, S. W., Y. Luo, Z. C. Zhao, et al., 2011: Debates on the cause of global warming. *Adv. Climate Change Res.*, **7**, 79–84. (in Chinese)
- Wang, S. W., Y. Luo, Z. C. Zhao, et al., 2013a: Global warming does not stall in the 21st century. *Progressus Inquisitiones de Mutatione Climatis*, **9**, 386–387, doi: 10.3969/j.issn.1673-1719.2013.05.013. (in Chinese)
- Wang, S. W., Y. Luo, Z. C. Zhao, et al., 2013b: Natural systems in changing climates. *Progressus Inquisitiones de Mutatione Climatis*, **9**, 440–445, doi: 10.3969/j.issn.1673-1719.2013.06.008. (in Chinese)
- Wang, S. W., Y. Luo, Z. C. Zhao, et al., 2014: How long will the pause of global warming stay again. *Progressus Inquisitiones de Mutatione Climatis*, **10**, 465–468, doi: 10.3969/j.issn.1673-1719.2014.06.011. (in Chinese)
- Zhao, T. B., and A. G. Dai, 2015: The magnitude and causes of global drought changes in the twenty-first century under a low-moderate emissions scenario. *J. Climate*, **28**, 4490–4512, doi: 10.1175/JCLI-D-14-00363.1.
- Zhou, T. J., L. W. Zou, B. Wu, et al., 2014: Development of earth/climate system models in China: A review from the coupled model intercomparison project perspective. *J. Meteor. Res.*, **28**, 762–779, doi: 10.1007/s13351-014-4501-9.
- Zhou, T. J., and X. L. Chen, 2015: Uncertainty in the 2°C warming threshold related to climate sensitivity and climate feedback. *J. Meteor. Res.*, **29**, 884–895, doi: 10.1007/s13351-015-5036-4.